Importance of Mesoscale Currents in AMOC Pathways and Timescales

IGOR KAMENKOVICH[a] AND ZULEMA GARRAFFO[b]

[a] *Rosenstiel School of Marine and Atmospheric Science, University of Miami, Miami, Florida*
[b] *IMSG at NOAA/EMC, College Park, Maryland*

ABSTRACT: The Atlantic meridional overturning circulation (AMOC) plays a key role in climate due to uptake and redistribution of heat and carbon anomalies. This redistribution takes place along several main pathways that link the high-latitude North Atlantic with midlatitudes and the Southern Ocean and involves currents on a wide range of spatial scales. This numerical study examines the importance of mesoscale currents ("eddies") in these AMOC pathways and associated time scales, using a highly efficient offline tracer model. The study uses two boundary impulse response (BIR) tracers, which can quantify the importance of the Atlantic tracer exchanges with the high-latitude atmosphere in the north and with the Southern Ocean in the south. The results demonstrate that mesoscale advection leads to an increase in the overall BIR inventory during the first 100 years and results in a more efficient and spatially uniform ventilation of the deep Atlantic. Mesoscale currents also facilitate meridional spreading of the BIR tracer and thus assist the large-scale advection. The results point toward the importance of spatial inhomogeneity and anisotropy of the eddy-induced mixing in several mixing "hotspots," as revealed by an eddy diffusivity tensor. Conclusions can be expected to assist evaluations of eddy-permitting simulations that stop short of full resolution of mesoscale, as well as development of eddy parameterization schemes.

KEYWORDS: Eddies; Meridional overturning circulation; Mesoscale processes; Mixing; Ocean circulation; Subgrid-scale processes; General circulation models

1. Introduction

Because of their enormous storage capacity, the oceans redistribute vast amounts of anomalous heat and carbon in the climate system and regulate long-term climate change. Model simulations further suggest that, on time scales of decades to centuries, the large-scale warming patterns are in large part controlled by the oceanic circulation, rather than the atmospheric processes (e.g., Marshall et al. 2015). The Atlantic meridional overturning circulation (AMOC), defined here as an overall meridional flow in the Atlantic Ocean, plays a particularly important role in Earth's climate and its variability (e.g., Broecker 1997; Stouffer et al. 2006). AMOC determines a large part of the oceanic uptake of heat and carbon and controls the depth to which these heat anomalies penetrate (e.g., Kuhlbrodt and Gregory 2012; Kostov et al. 2014). Studies further demonstrate that AMOC is different from a large-scale stationary "conveyor belt," but is rather a complex three-dimensional pattern (e.g., Lumpkin and Speer 2007), characterized by variability on a wide range of spatial and time scales (e.g., Smeed et al. 2014; Yeager and Danabasoglu 2014). In this paper, we will use high-resolution model simulations of dynamically passive tracers to better characterize the role of mesoscale currents [$O(10–100)$ km or "eddies" hereafter] in advective AMOC pathways and associated time scales.

Distribution of heat and anthropogenic carbon anomalies by AMOC is governed by complex interactions between the along- and cross-isopycnal advection and small-scale mixing. Diapycnal mixing can influence the midlatitude stratification and high-latitude deep-water formation (e.g., Munk 1966;

Gnanadesikan 1999), which is manifested in strong sensitivity of AMOC to vertical mixing in numerical simulations (e.g., Bryan 1987). In an alternative, semiadiabatic regime (Marshall and Radko 2003), the water is moving strictly along isopycnals, forced by mass exchanges with the surface mixed layer. Several model-based studies suggest significance of a semiadiabatic AMOC branch (Gnanadesikan 1999; Samelson 2004; Sevellec and Fedorov 2011; Toggweiler and Samuels 1998; Wolfe and Cessi 2010). Radko et al. (2008) describe this branch as a "push–pull mode" of AMOC and demonstrate that it explains most of the total AMOC transport and its variability (see also Grist et al. 2009; Han et al. 2013). The deep portion of the Atlantic push–pull mode is driven by the mass exchanges with the Southern Ocean and the deep mixed layer in the Northern high latitudes (Kamenkovich and Radko 2011; Radko et al. 2008). The share of the semiadiabatic component can be expected to be even larger in nature, since numerical simulations used in AMOC studies tend to have high values of diapycnal diffusivity, which are not supported by direct observational estimates (Ledwell et al. 1993; Toole et al. 1994).

The advective pathways outside of the mixed layer and convective sites are determined by interactions between large-scale currents and mesoscale eddies. Lateral transfer of buoyancy by mesoscale eddies have indeed been shown to play an active role in maintaining midlatitude stratification (Cessi and Fantini 2004; Henning and Vallis 2004; Radko and Marshall 2004) and propagation of the transient tracers (Booth and Kamenkovich 2008; Kamenkovich et al. 2017). In non-eddy-resolving simulations, the distributions of tracers and density is highly sensitive to horizontal resolution and parameterization of eddy-induced transports (e.g., Doney et al. 2004; Dutay et al. 2002; Gnanadesikan et al. 2013; Gnanadesikan

Corresponding author: Igor Kamenkovich, ikamenkovich@miami.edu

et al. 2004; Sen Gupta and England 2004). Specifically, numerical simulations show strong sensitivity of the oceanic uptake of heat (e.g., Huang et al. 2003) and anthropogenic carbon (Gnanadesikan et al. 2015) to the horizontal and isopycnal eddy mixing.

The evolution of tracer anomalies entering the Atlantic from the surface and the Southern Ocean can be described as a response to the corresponding surface and lateral boundary forcing. A convenient way of calculating such a response involves the boundary impulse response (BIR) function (Haine and Hall 2002; Holzer and Hall 2000; Khatiwala et al. 2001). For example, if the BIR is calculated from a response to an instant impulse at a given time and infinitely small surface area, it is equivalent to a Green's function. Such a Green's function can in theory be calculated for all possible surface impulses. The concentration of an arbitrary tracer that enters the ocean through the surface and has no internal sources and sinks can then be derived from the tracer distribution at the surface and a complete set of BIRs. In practice, however, both the duration of the impulse and the source region area are made finite (e.g., Haine and Hall 2002; Khatiwala et al. 2001; Peacock and Maltrud 2006). For example, Khatiwala et al. (2009) used this approach to reconstruct the spatial distribution of anthropogenic carbon inventory. Mixing by eddies and small-scale processes can substantially modify the propagation of a pulse. Waugh and Hall (2005) used an idealized model of a deep western boundary current to demonstrate that the arrival of the BIR peak value (the "pulse") can be significantly delayed by the mixing between the boundary current and the oceanic interior. Time scales in their model also strongly depend on the tracer time history at the origin, particularly in the intermediate mixing regime with comparable advective and mixing time scales [Peclet number of $O(1)$]. Simulations of an ensemble of BIRs in a realistic global eddy-resolving model by Maltrud et al. (2010) exhibit vigorous mesoscale variability in BIR distributions but also demonstrate a remarkable agreement between ensemble members, especially at long time scales. In this paper, we will extend the previous studies and seek to isolate the importance of mesoscale eddies in AMOC advection by comparing two specific BIR simulations with and without mesoscale currents. A complete set of BIRs will not, however, be calculated.

The eddy-induced mixing of oceanic tracers is spatially inhomogeneous and anisotropic (e.g., Abernathey and Marshall 2013; Bachman et al. 2020; Kamenkovich et al. 2021; Rypina et al. 2012), which has been shown to be important for tracer distributions. For example, Booth and Kamenkovich (2008) used high-resolution simulations of the chloroflourocarbon-11 (CFC-11) with and without eddies to demonstrate the importance of eddy mixing in several key locations and show that eddies fill the interior of the Atlantic subpolar gyre with CFC-11, dispersing the tracer away from the mean pathways of the North Atlantic and Labrador currents; the eddies also act to limit vertical penetration of the tracer and decrease the convective removal of CFC-11 from the surface. Kamenkovich et al. (2017) used high-resolution simulations of a BIR tracer to study the interactions between the mean and eddy-induced advection in the Southern Ocean and show that the eddies

spread the ventilation signal away from the mean pathways, which inhibits the removal of tracers from the Atlantic into the Indian Ocean and enhances the ventilation of the Atlantic southern subtropical gyre. Finally, the anisotropy of the mesoscale currents and the resulting eddy-induced transport are also important for tracer distribution within subtropical and subpolar gyres (Kamenkovich et al. 2015).

In this paper, we will use an offline tracer model of the Atlantic basin, whose high spatial resolution and numerical efficiency enables a direct inquiry into the importance of eddies in tracer distributions. We use BIR tracers, propagating from the North Atlantic surface and from the lateral southern boundary, to study the pathways and time scales associated with AMOC. We do not calculate transient time distribution (TTD) or ideal age of AMOC waters in this study, because it would require multiple simulations in a global domain. Instead, we focus on the importance of eddies in one realization of BIR evolution, assuming the results are representative (see Maltrud et al. 2010). The model is described in section 2. The intensity of the eddy-induced stirring is quantified by a time-mean, but space-dependent diffusivity tensor in section 3. Section 4 will compare the results in simulations with the full flow (hereafter FULL_ADV) and mean (large scale, hereafter, MEAN_ADV) flow only, which serves to isolate the direct importance of the eddy-induced tracer transports. Conclusions are drawn in section 5.

2. Atlantic Offline Tracer Model (AOTM)

The Atlantic Offline Tracer Model (AOTM) uses precalculated velocities, layer thicknesses, and vertical diffusivities to solve the tracer equation. The formulation is similar to the one used in the Southern Ocean model by Kamenkovich et al. (2017) and will be only briefly described here. The physical variables are calculated in a separate "online" simulation with the Hybrid Coordinate Ocean Model (HYCOM; Bleck 2002; Chassignet et al. 2003; Halliwell 2004). HYCOM was originally based on the Miami Isopycnic Ocean Model (MICOM; Bleck et al. 1992) and uses isopycnal coordinates in the open ocean and below the mixed layer. The online simulation used by the AOTM has a global domain with 1/12° spatial resolution; the horizontal grid is rectilinear south of 47°N (being equatorial Mercator except in the high southern latitudes) followed by an Arctic bipolar patch. The vertical grid has 41 hybrid layers: isopycnal in the deep ocean, z levels in the ocean interior near the surface, and sigma coordinates near the coasts. The horizontal resolution (~3.2–8 km at 70°–30°S) is among the highest available today, but still falls short of accurate resolution of the small-scale eddies of the size of the first internal Rossby deformation radius (~10–20 km at these latitudes; Chelton et al. 1998). Our focus is, therefore, on eddies with scales of larger than approximately 20–50 km. The potential density is referenced to the 20-MPa surface (Chassignet et al. 2003; Sun et al. 1999). The model employs the KPP vertical mixing scheme (Large et al. 1994), whose diapycnal/vertical coefficients are saved and used in AOTM.

The spinup for the base calculation was completed at the Naval Research Laboratory (NRL) starting from the observed

stratification. The model was forced with monthly ECMWF (ERA-40) forcing fields plus 3- or 6-hourly anomalies obtained from the Navy Operational Global Atmospheric Prediction System (NOGAPS). The ocean model is coupled with the Los Alamos Sea Ice model (CICE). At this resolution, the model has been used extensively at the NRL. Typically, a climatological spinup is used to initialize interannual simulations; see http://www.hycom.org for more details. The present climatological simulation was spun up at NRL for 15 years and used for their Global Ocean Forecast System. This simulation was run for additional 5 years and 16 days in order to save all the required fields, including instantaneous layer thicknesses and vertical diffusivities.

Offline tracer simulations were originally formulated by R. Bleck (2006, personal communication); early offline tracer simulations are presented in Sun and Bleck (2001). The offline tracer model solves the prognostic equation for the tracer concentration c within a layer of thickness $\Delta z(x, y, t)$ (Kamenkovich et al. 2017):

$$\frac{\partial(c\Delta z)}{\partial t} = -\nabla \cdot (\mathbf{U}c) - \partial(\omega c) + \nabla \cdot A_h \Delta z \nabla c + \mathfrak{D}(c), \quad (1)$$

where $\mathbf{U}$ is the layer volume flux (velocity times layer thickness), $\mathfrak{D}(c)$ is the diapycnal/vertical mixing and $\partial(\omega c)$ is the difference between the vertical fluxes through the top and bottom of each layer. The vertical volume flux is diagnosed from the continuity equation by

$$\partial(\omega) = -\left\{\nabla \cdot \mathbf{U} - \frac{\partial \Delta z}{\partial t}\right\}. \quad (2)$$

Daily mean layer volume fluxes are used to compute the first term on the right-hand sides of (1) and (2), whereas the change in the layer thickness [second term on the right-hand side of Eq. (2)] is calculated from the instantaneous layer thicknesses. The conservation of mass is, therefore, exact in the daily mean sense. The diapycnal/vertical mixing $\mathfrak{D}(c)$ is calculated from daily mean diffusivities saved in the online simulation. The term A_h is the horizontal/isopycnal Laplacian diffusivity required for numerical stability; its value is $0.01\Delta x$ in the control simulation, with Δx being the horizontal grid spacing. The explicit diffusivity is significantly smaller than the eddy-induced diffusivity discussed in section 3. Equation (1) is solved using a three-dimensional, fourth-order advection scheme with flux-corrected transport (Zalesak 1979). The time step is 1 h. AOTM is forced with 5 years of data, which are repeated every five years. To smooth a transition from the end of each 5-yr cycle to the beginning of the next one, blended values are used for all forcing fields for the first 16 days of year 1. These blended values are calculated as a weighted average between first 16 days of year 1 and year 6.

To estimate the error due to the use of daily values in the offline calculations of the advective and vertical-mixing terms, we carried out online and offline simulations of the same tracer. The tracer is initialized to unity on the first day of year 4 in the region between longitudes 74.6° and 21.9°W, between latitudes 30.2° and 36.8°N, and below the model layer 24; this layer depth varies between approximately 300 and 1000 m. At
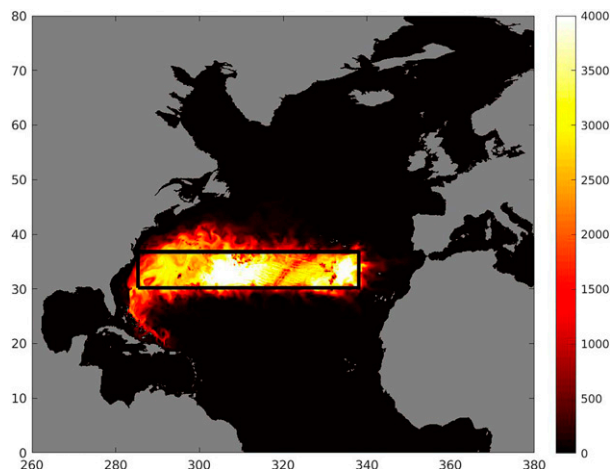

FIG. 1. An idealized tracer used in the test of the offline approach, shown at the end of the 2-yr integration. The black frame shows the initial distribution.

the end of year 4, these results are visually indistinguishable from the offline simulations with AOTM simulations initialized in the same way (Fig. 1). We define the spatial standard deviation of a quantity g in a model layer as follows:

$$\text{SD}(g) = \left[\frac{1}{V}\int g^2 \Delta z dx dy - \left(\frac{1}{V}\int g\Delta z dx dy\right)^2\right]^{1/2}, \quad (3)$$

where $V = \int \Delta z \, dx dy$ is the volume of the layer and g is smoothed by the running-mean $1° \times 1°$ filter (to remove grid-scale errors). A relative bias $e = \text{SD}(c_{\text{offline}} - c_{\text{online}})/\text{SD}(c_{\text{online}})$ remains between 2% and 9% in all layers. For the depth-integrated tracer values (tracer inventory), which will be the main variable discussed in this study, the errors are significantly smaller, with the relative bias e less than 0.6%. Since even a small error in the position of the center of mass of a tracer patch could lead to large values of e, we also compared the tracer variance in both simulations. In the offline simulation, $\text{SD}(c_{\text{offline}})$ remains within 4% of the online value $\text{SD}(c_{\text{online}})$ in each layer below layer 24. Similar to Kamenkovich et al. (2017), we conclude that the errors due to the use of daily fields are sufficiently small to warrant the use of AOTM for simulations of passive tracers.

3. Mesoscale variability

The main goal of this study is to establish the importance of mesoscale stirring in tracer distribution. We begin with the eddy-induced transport tensor $\mathbf{K}$ in the FULL_ADV simulation, which will serve as a measure of eddy activity and its significance for tracer stirring and mixing. In the following part of the study, we will examine the importance of the eddy-induced advection by using separate experiments MEAN_ADV, in which the mesoscale variability is removed from the lateral volume fluxes and layer thickness.

Both approaches require a meaningful definition of the mesoscale. The definition is, however, not unique, because a clear scale separation between the mesoscale and seasonally varying large-scale fields does not exist. It is hard to design a method that would guarantee a complete removal of mesoscale processes from the 5 years of our model simulations. After a careful comparison of several approaches, we settled on a combination of time and spatial averaging: The data are first averaged in time and then smoothed spatially with a 25×25 point moving area average filter, which is aligned with the latitude–longitude grid. Our analysis shows that this method removes the mesoscale variability more effectively than, for example, spatial smoothing alone, time averaging or smoothing in time. For example, our attempts to retain the climatological annual cycle by low-pass filtering all fields in time failed to remove a significant portion of mesoscale eddies, most notably, the Agulhas rings. Note that, although the spatial smoothing we use in this simulation broadens the deep western boundary current (DWBC) and reduces its peak speed, the DWBC volume transport is conserved.

The treatment of the diapycnal/vertical mixing in MEAN_ADV is even more challenging. Although the main focus of this study is on semiadiabatic pathways below the surface mixed layer, the injection of the BIR tracer into these pathways depends on the vertical mixing in the upper ocean. Since the vertical diffusion within the mixed layer tends to be particularly strong in isolated regions of the North Atlantic, spatial or temporal smoothing would artificially increase these injection rates. To avoid this bias, we chose to use the full, unfiltered vertical/diapycnal mixing. We also tested two filtered values of the vertical diffusivity: (i) time-mean and spatially smooth diffusivity and (ii) diffusivity that is smoothed in time, but not in space. Although the main conclusions from these two tests remain the same as in our main MEAN_ADV simulation, these two settings resulted in a noticeably faster decline in the global BIR inventory.

a. Eddy diffusivity tensor

The calculation of the eddy transport tensor is based on the flux–gradient relation between the lateral eddy-induced tracer flux $\mathbf{F}_e$ and the large-scale tracer gradient:

$$\overline{\mathbf{F}_e} = -\mathbf{K}\overline{\Delta z}\nabla\langle c\rangle , \qquad (4)$$

where $\langle \ldots \rangle$ denote the 25-point running-mean 2D filter and the overbar stands for the 5-yr average. The lateral direction is defined as horizontal in the surface mixed layer and isopycnal in the oceanic interior below it. The 2×2 transport tensor $\mathbf{K}$ is calculated in each model layer separately and stands for the lateral transport coefficient tensor; the tensor depends on location (i.e., is inhomogeneous) but is constant in time by definition. The methods used in this section are the same as in Kamenkovich et al. (2021) except that they used the time-dependent $\mathbf{F}_e$ in (4). The use of time-independent transport tensor here simplifies the discussion and reduces numerical errors but ignores potentially important temporal fluctuations in the tensor.

The eddy flux $\mathbf{F}_e$ is the difference between the full flux and the flux due to the large-scale advection (used in MEAN_ADV):

$$\overline{\mathbf{F}_e} = \overline{\mathbf{U}c} - \overline{\langle\mathbf{U}\rangle}\,\overline{\langle c\rangle}. \qquad (5)$$

Note that in the isopycnal model layers, the large-scale layer volume flux $\langle\overline{\mathbf{U}}\rangle$ includes the eddy-induced layer volume fluxes, which represents the effects of eddies on density (Gent and McWilliams 1990). These fluxes are not discussed in this paper.

The flux–gradient relation (4) can be solved exactly for a given pair of tracers. Kamenkovich et al. (2021), however, found that in this case the tensor depends on the tracers used for the calculations; see also Bachman et al. (2020) and Sun et al. (2021) for the same conclusion. This tracer dependence makes the solution nonunique and casts doubts on applicability of the eddy diffusivity tensor, which is assumed to be tracer-independent in (4). A practical approach to this problem is to use multitracer ensemble-averaged estimates of eddy diffusivity (Abernathey et al. 2013; Bachman et al. 2020, 2017). In this study, we follow the same logic and calculate the transport tensor in (4) as a least squares fit for four independent tracers, which are initially vertically uniform but have different horizontal profiles (see the appendix). Eighteen overlapping 110-day-long simulations are carried out, with each consecutive segment starting 10 days before the end of the previous one; only the last 100 days of each simulation are used in the calculations.

Prior to solving (4), we remove the nondivergent ("rotational") flux component (Haigh et al. 2020; Jayne and Marotzke 2002; Marshall and Shutts 1981), which does not affect tracer distribution but tends to dominate $\mathbf{F}_e$. The rotational component is calculated for each tracer flux separately, using the Helmholtz decomposition (Lau and Wallace 1979):

$$\nabla \cdot \mathbf{F}_e = \nabla^2\Phi, \; \nabla \times \mathbf{F}_e = \nabla^2\Psi,$$

$$\mathbf{F}_e = \mathbf{F}_{\text{div}} + \mathbf{F}_{\text{rot}},$$

$$\mathbf{F}_{\text{div}} = \nabla\Phi, \; \mathbf{F}_{\text{rot}} = \nabla \times \Psi. \qquad (6)$$

In the above equations, Φ is the potential that corresponds to the divergent flux component $\mathbf{F}_{\text{div}}$, and Ψ is the streamfunction that corresponds to the rotational component $\mathbf{F}_{\text{rot}}$. The separation of $\mathbf{F}_e$ into the rotational and divergent components via the Helmholtz decomposition is, unfortunately, not unique and depends on the boundary conditions (Fox-Kemper et al. 2003; Jayne and Marotzke 2002; Maddison et al. 2015; Roberts and Marshall 2000), which are known for the total $\mathbf{F}_e$ but not for its rotational and divergent components, separately. The ambiguity in boundary conditions leads to uncertainty in the transport tensor estimates (e.g., Kamenkovich et al. 2021). Because of the open boundaries in our domain, we chose to use the optimization technique with Tikhonov regularization (Li et al. 2006), which minimizes those components in $\mathbf{F}_{\text{div}}$ and $\mathbf{F}_{\text{rot}}$ that are both nonrotational and nondivergent; see the appendix. These opposing components cancel each other

in $\mathbf{F}_e$ but cause ambiguity in defining $\mathbf{F}_{\text{div}}$ and $\mathbf{F}_{\text{rot}}$ (Maddison et al. 2015). Note that for an exact solution of (4), the divergence of $\mathbf{F}_{\text{div}}$ and $\mathbf{F}_e$ are the same $\nabla \cdot \mathbf{F}_{\text{div}} = \nabla \cdot \mathbf{F}_e$ regardless of the boundary conditions used in the Helmholtz decomposition. The transport tensor $\mathbf{K}$ will, however, be sensitive to the particular definition of $\mathbf{F}_{\text{div}}$.

The transport tensor $\mathbf{K}$ can be separated into the symmetric and antisymmetric components, which have different physical meanings. The symmetric part $\mathbf{S}$ stands for a diffusive process affecting the tracer variance, while the antisymmetric component $\mathbf{A}$ represents advective effects. Note that the corresponding fluxes $\mathbf{S}\Delta z \nabla c$ and $\mathbf{A}\Delta z \nabla c$ will both have divergent and rotational components, unless the eddy-induced stirring is isotropic and homogeneous (Kamenkovich et al. 2021).

The diffusion tensor $\mathbf{S}$ can be further modified to show the preferred direction and efficiency of diffusion,

$$\mathbf{S} = \begin{bmatrix} S_{11} & S_{12} \\ S_{12} & S_{22} \end{bmatrix} = \mathbf{I}_R \begin{bmatrix} \lambda_1 & 0 \\ 0 & \lambda_2 \end{bmatrix} \mathbf{I}_R^{\mathrm{T}}, \quad (7)$$

where

$$\mathbf{I}_R = \begin{bmatrix} \cos\theta & -\sin\theta \\ \sin\theta & \cos\theta \end{bmatrix}$$

is a rotation matrix, θ defines the direction of the maximal diffusion, and $\lambda_{1,2}$ are the corresponding eigenvalues (diffusivities). We define λ_1 as the largest diffusivity and λ_2 as the smallest diffusivity.

Similar to the time-dependent diffusion tensor diagnosed from the same flow (Kamenkovich et al. 2021), the time-mean diffusion tensor in this study exhibits pairs of positive and negative eigenvalues, $\lambda_1 > 0$ and $\lambda_2 < 0$, in the oceanic interior (Fig. 2). This "polarity" results from eddies acting to bring tracer contours closer together in one direction while stretching the contours in the direction perpendicular to it (Haigh et al. 2021a; Sun et al. 2021). Although this eddy-induced filamentation can still correspond to net downgradient transfer of variance (Haigh and Berloff 2021) or be balanced by large-scale advection in the full flow, negative λ_2 can lead to numerical instability if implemented in numerical models. In addition, the numerical stability is compromised by isolated extreme values in λ_1, resulting from weak tracer gradients $\nabla \langle c \rangle$. For these two reasons, our attempts to use tensor $\mathbf{K}$ and its isotropic approximation in MEAN_ADV led to numerical instability and unphysical results. The investigation of the utility of representing eddies by the comprehensive tensor $\mathbf{K}$ is left for future studies with coarse-resolution models, and the analysis here is restricted to the description of the spatial inhomogeneity in the transport tensor.

Both eigenvalues decrease in magnitude with depth (Fig. 2), which is expected, given the decrease in the eddy kinetic energy (not shown). The lateral variability is even stronger, and the magnitude of λ_1 changes by two orders of magnitude from the relatively quiet eastern part of the domain to very energetic western regions. Not surprisingly, the diffusivity is large around the path of the Gulf Stream and deep western boundary current. A particularly strong local maximum in the eddy-induced tracer stirring is found around approximately 35°N in the deep western part of the domain, which will have important implications for the propagation of the BIR tracer from the north. Another region of elevated diffusivity λ_1 is the South Atlantic, which will be important for meridional spreading of the BIR tracer from the south boundary of the domain. Similarly strong spatial variations were reported in the previous estimates of the lateral diffusivity (e.g., Bachman et al. 2020; Haigh et al. 2020). Explanation of the origins of this variability is challenging because of the complexity of the flow and is beyond the scope of this paper, although large diffusivities can be expected in the regions where the isopycnals are steep, such as vicinity of the western boundary and the Southern Ocean.

Another important characteristic of the diffusivity tensor $\mathbf{S}$ is the direction of the maximal eddy-induced dispersion (with the diffusivity λ_1), shown by the gray lines in Fig. 2. This direction tends to be zonal in the oceanic interior between approximately 20°S–30°N, away from the coasts and major topographic features (Fig. 2a). This predominantly zonal direction of the eddy-induced transport is consistent with previous Lagrangian estimates of the diffusivity tensor (Kamenkovich et al. 2015; Rypina et al. 2012). The direction of the maximal dispersion is, in contrast, nonzonal in most of the domain, especially north of 35°N and south of 20°S, near the "mixing hotspot" at 35°N and in the vicinity of the western boundary (Fig. 2). In particular, deep layers tend to correspond to mostly nonzonal transport. The reported direction of the maximal dispersion will have two important implications for BIR distributions. Consistent with the idealized "leaky pipe" model, the eddies will spread the tracers zonally away from the western boundary, and these effects will be particularly important in the interior and far from topography. Second, the eddies will also facilitate meridional propagation of BIR tracers from both the north and south source regions, and these effects will be particularly important in the subpolar region, South Atlantic and near the western boundary.

The antisymmetric component $\mathbf{A}$ of the transport tensor corresponds to advective effects of eddies on tracers, with the streamfunction A_{12} and eddy-induced tracer velocities (EITV) $\mathbf{u}_A = (u_A, v_A)$:

$$\mathbf{A} = \begin{pmatrix} 0 & -A_{12} \\ A_{12} & 0 \end{pmatrix}, \quad u_A = -\frac{\partial A_{12}}{\partial y}, \quad v_A = \frac{\partial A_{12}}{\partial x} \quad (8)$$

EITV multiplied by the large scale layer thickness $\overline{\langle \Delta z \rangle}$ are shown in Fig. 3, together with the large-scale layer volume fluxes $\overline{\langle \mathbf{U} \rangle}$. EITV are smaller in magnitude than $\overline{\langle \mathbf{U} \rangle}$ in most of the domain, except the mixing hotspot near 35°N and the western boundary region. In the latter locations, v_A tends to be southward, which means that eddies will facilitate southward spread of BIR tracers in the deep layers. Note that EITV and $\overline{\langle \mathbf{U} \rangle}$ have different physical meaning and properties. The term $\overline{\langle \mathbf{U} \rangle}$ represents the actual large-scale transport of water within each layer, both due to the large-scale velocities and eddies; divergence of this transport leads to changes in the layer thickness and generates diapycnal exchanges. In contrast, EITV describe the advective part of the tracer transport, do not affect density, and are nondivergent (e.g., Haigh et al. 2021b). The
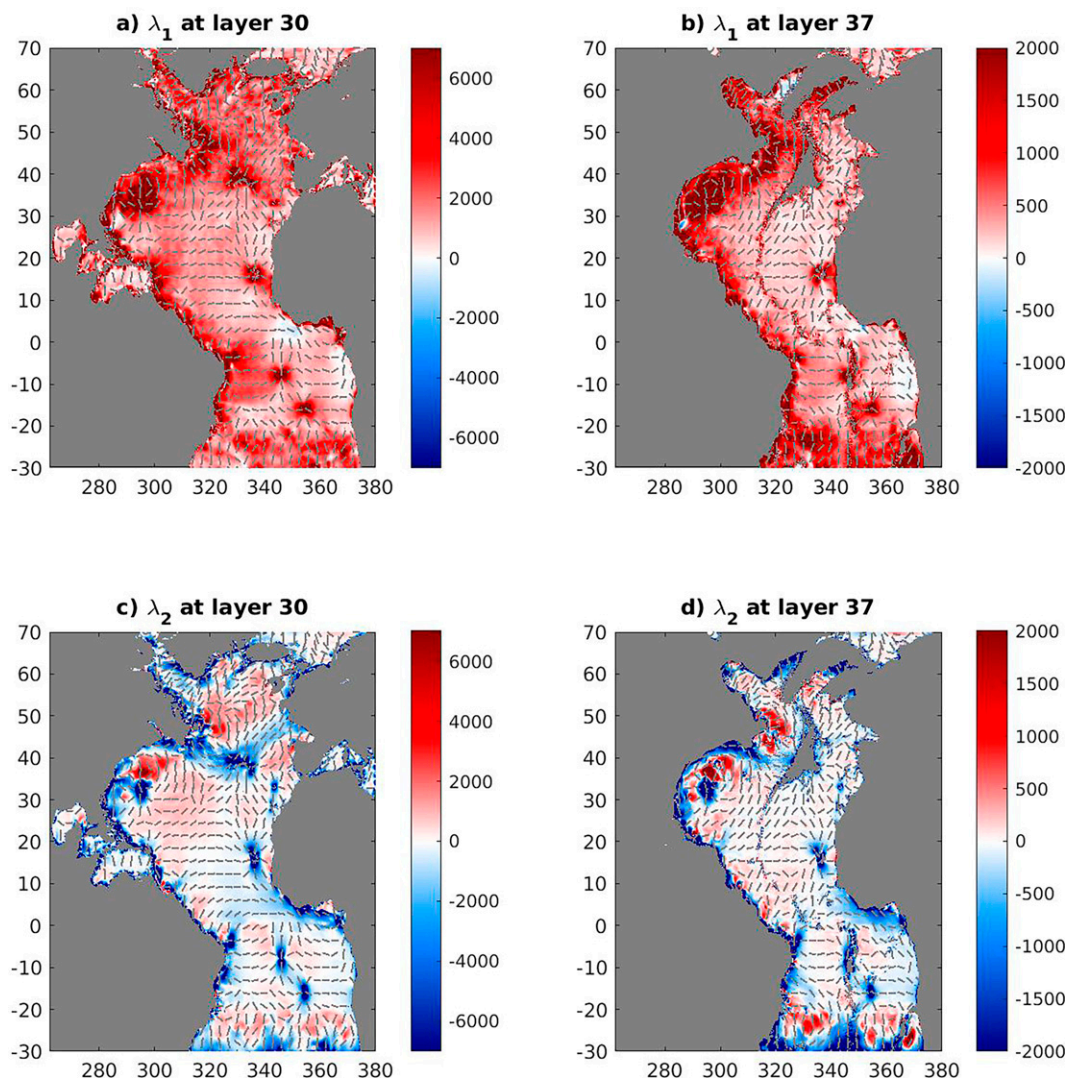
FIG. 2. Eigenvalues ($m^2\,s^{-1}$) of the diffusivity tensor **S**: (a),(b) λ_1 (largest) and (c),(d) λ_2 (smallest) eigenvalues (color shading) and the direction of the first eigenvector (lines, at every 40th point in each direction). Two model layers are shown: (left) layer 30 (zonal-mean depth of 388–1307 m) and (right) layer 37 (zonal-mean depth of 1280–3430 m); the zonal average depths of these layers are also shown in Fig. 5.

relative importance of the advective (tensor **A**) and diffusive (tensor **S**) processes depends on the large-scale tracer structure. For example, consider a highly idealized case of a linear tracer profile with constant $\nabla\langle c\rangle$. Since all second derivatives in $\langle c\rangle$ are zero, the advective transport by EITV can be expected to dominate the tracer distribution.

4. Simulations of the BIR tracers

In this study we consider two BIR tracers, one originating from the surface area in the North Atlantic (north of 50°N, NBIR hereafter), and another coming from the southern lateral boundary of the domain (at 30°S, SBIR hereafter). These BIR tracers correspond to propagation of pulses from the corresponding boundaries, but do not constitute a complete set

of Green's functions. During year 1, NBIR is set to unity at the surface north of 50°N and to zero south of this latitude; starting at year 2, the tracer is set to zero over the entire surface boundary. Similarly, SBIR is set to unity at the southern boundary of the model domain during year 1 and to zero starting at year 2. Surface fluxes of SBIR are always zero. There are no other sources and sinks in the rest of the domain. Both tracers are nondimensional. We carried out only one simulation for each tracer and use it to describe the propagation of a boundary forced signal within AMOC.

a. NBIR simulations

During the first year, when the NBIR tracer is set to unity at the surface north of 50°N, the tracer quickly fills the mixed layer and begins spreading into the rest of the domain. As the
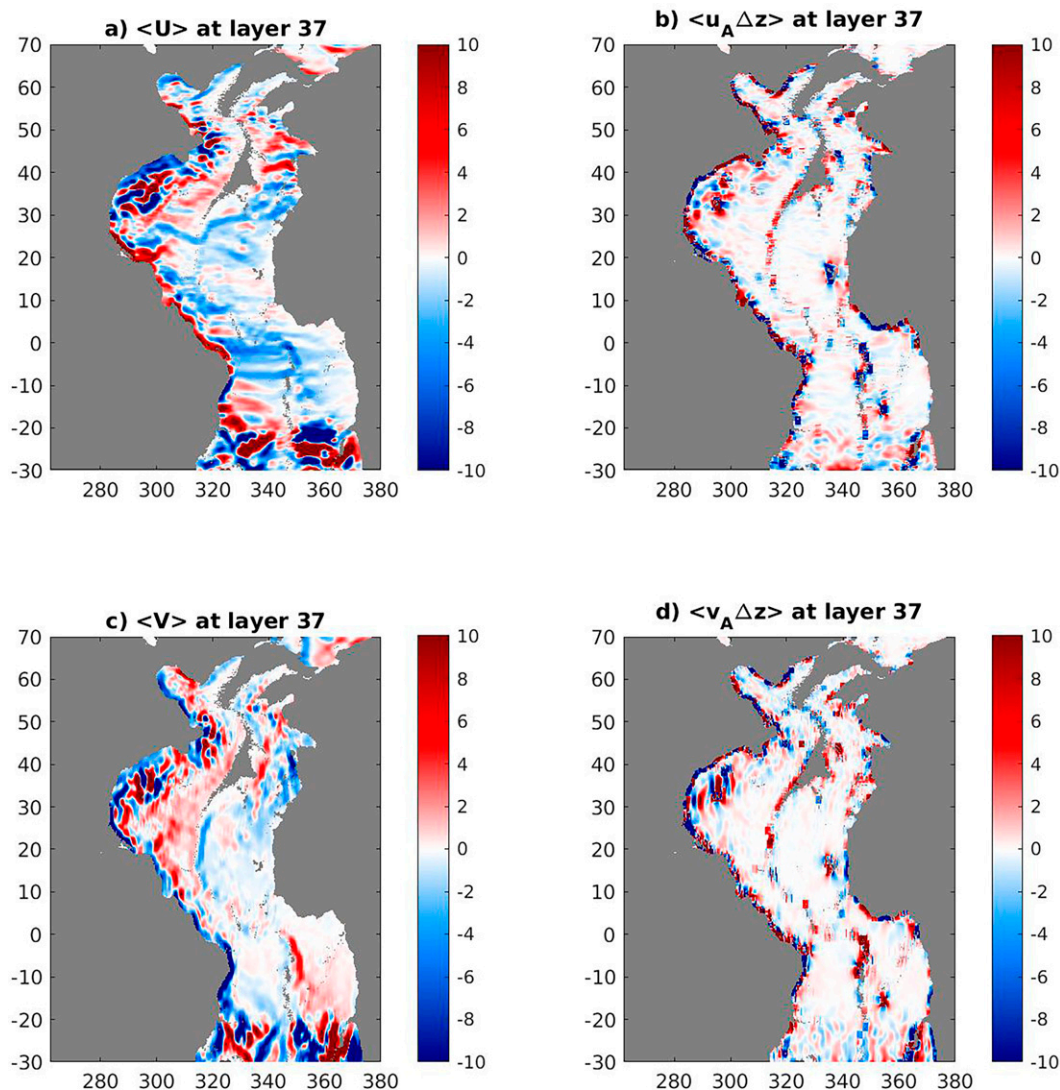
FIG. 3. Large-scale layer volume flux $\overline{\langle U \rangle}$ and EITV multiplied by the large scale layer thickness $\overline{\langle \Delta z \rangle}$ at layer 37 (zonal-mean depth of 1280–3430 m): (a) zonal flux $\overline{\langle U \rangle}$; (b) eddy induced zonal velocity times layer thickness $\langle u_A \overline{\langle \Delta z \rangle} \rangle$; (c) meridional flux $\overline{\langle V \rangle}$; (d) eddy induced meridional velocity times layer thickness $\langle v_A \overline{\langle \Delta z \rangle} \rangle$. Units are $m^2 \, s^{-1}$.

tracer is being removed from the surface starting at year 2, the total tracer inventory begins to decline while the tracer also spreads around the entire domain. The decrease in the inventory is fast initially, but then slows down as less and less tracer-rich waters come in contact with the surface. If we neglect tracer exchanges with regions outside of the model domain, the change in the total tracer inventory will be determined by the tracer loss from the surface. The tracer removal rate from the surface can be assumed to be proportional to the tracer concentrations c_{ML} within the surface mixed layer,

$$\frac{\partial}{\partial t} \iiint c \, dV \approx -\alpha \iint c_{ML} \, dS. \qquad (8)$$

The parameter α in the above relation is the removal speed that depends on how fast the tracer within the mixed layer is resupplied to the surface due to vertical mixing and advection. In the limit of very strong vertical mixing, the tracer is instantly homogenized within the mixed layer and $\alpha = \Delta z / \Delta t$, where Δz is the thickness of the topmost model layer (1 m) and Δt is the time step (1 h). In the absence of lateral advection and stirring, the tracer stays within the mixed layer and $c = c_{ML}$. Assuming that the mixed layer has a uniform thickness of $h = 300$ m, the tracer concentration is then decaying exponentially with an e-folding time of $\Delta t(h/\Delta z) = O(10)$ days. The tracer response in this case is indeed a short-lived pulse that quickly dissipates with time. The advection decreases c_{ML} reducing the removal rate, the right-hand side of (8). The resulting decline in the total

inventory is significantly slower than in the case with no advection and is different from exponential. For example, the time scale $T_r = \iint c \, dV [-(\partial/\partial t) \iint c \, dV]^{-1}$, which would be an *e*-folding time scale $1/\alpha$ if the decay were purely exponential, changes from approximately 2.5 years to almost 34 years from year 1 to year 25 for FULL_ADV. The decay time scale T_r is also very sensitive to the lateral advection. In MEAN_ADV, the lack of eddy-induced stirring increases the surface removal rate and the parameter T_r is shorter than in FULL_ADV, varying from 2 years to approximately 22 years. As the result, the total inventory of NBIR in MEAN_ADV is noticeably smaller than in FULL_ADV, with the ratio between two inventories being as large as almost 4.0 by the end of the 100-yr simulation.

With time, the BIR pulse in both simulations leaves the mixed layer in the high latitudes and propagates southward within the WBC (Figs. 4a,b). The horizontal distribution and associated time scales are, however, different between the two runs. The tracer is subject to lateral mixing by mesoscale eddies in the FULL_ADV simulation, which removes the BIR tracer from the mean pathway and spreads it into the interior (Maltrud et al. 2010; Waugh and Hall 2005). The eddy-induced diffusivities (Fig. 2) indeed show predominantly zonal downgradient tracer transport in large parts of the mid- and low-latitude interior. According to the idealized leaky pipe model in Waugh and Hall (2005), the zonal exchange between the WBC and the deep interior broadens the BIR pulse and slows its southward propagation. How different is AMOC in our study from the idealized leaky-pipe solution?

Propagation of the pulse in the FULL_ADV case is indeed slower than in MEAN_ADV north of the Gulf Stream. For example, the NBIR pulse arrives at the Cape Hatteras (35°N) during year 6 in MEAN_ADV (Fig. 5a), which implies a propagation speed of approximately 0.01 m s^{-1}, whereas the NBIR peak in the FULL_ADV case arrives at this latitude later, during year 10. For comparison, the speed of DWBC in MEAN_ADV is between 0.02 and 0.05 m s^{-1}, and peak speeds are even faster in FULL_ADV. According to the leaky-pipe model, the difference between the WBC and NBIR propagation speeds can be explained by lateral tracer spreading in the vicinity of the western boundary, which is driven by the eddy-induced mixing in FULL_ADV and large-scale recirculation in FULL_ADV and MEAN_ADV. The peak passage is also more spread out in time in FULL_ADV (Figs. 5a,b), which is qualitatively consistent with the analytical TTD derived for the leaky-pipe model (Waugh and Hall 2005).

After reaching the Cape Hatteras, the southward propagation of the tracer pulse slows down in both simulations (Figs. 4a,b), which is possibly explained by the interaction of the DWBC with the northeastward flowing Gulf Stream. At the same time, this region is a hotspot of eddy-induced mixing, according to our analysis of the eddy diffusion and advective tensors (Figs. 2 and 3), since both tensors exhibit large meridional spreading in this region. The eddies thus facilitate propagation of the NBIR pulse southward of 35°N in FULL_ADV, and their absence explains a much slower propagation of the pulse in MEAN_ADV. As a result, the NBIR pulse arrives at 25°N during year 22 in FULL_ADV and only during

year 40 in MEAN_ADV (Figs. 5c,d). On later stages, the tracer fills the abyssal plain, and the region corresponds to a local maximum in the BIR inventory in both simulations (Figs. 4g,h).

The spreading of the NBIR tracer to the east of the mid-Atlantic ridge is slower than in the west and the difference between FULL_ADV and MEAN_ADV simulations is less pronounced there (Figs. 4e–h). At the depths shallower than the top of the ridge, the tracer is advected eastward from the western Atlantic within multiple zonal jets (Fig. 3a; Kamenkovich et al. 2009; Maximenko et al. 2008) and by mesoscale eddies (Figs. 2 and 3). The signature of the jet advection is mostly observed in MEAN_ADV in the model layers 1 to 34, which correspond to the average depth of approximately 1900–2200 m (not shown), but is also visible in Figs. 4c–f. The eddy-induced transport is also predominantly zonal at these depths, south of approximately 30°N (Fig. 2a). Other pathways include the eastward deep equatorial current (Figs. 4e,f). In the deeper layers, eastward propagation of the tracer is impeded by the mid-Atlantic Ridge, although the tracer can still get through multiple fracture zones. Once the tracer ends up in the eastern part of the basin, it slowly spreads southward, forming a secondary pulse. This secondary pulse in FULL_ADV moves noticeably faster than in MEAN_ADV and reaches the tropics by year 100, whereas the eastern pulse stays north of approximately 25°N in MEAN_ADV. The NBIR distribution south of the equator by year 100 are qualitatively similar between the FULL_ADV and MEAN_ADV simulations (Figs. 4g,h).

The broad NBIR pulse in the FULL_ADV case extends farther south than in MEAN_ADV at most depth levels, as is evident in the depth–latitude (zonally integrated) plots (Fig. 6). The difference becomes particularly large by year 100, when 30% of the total NBIR inventory is found south of the equator in FULL_ADV, compared to only 17% in MEAN_ADV. These depth–latitude plots also exhibit a two-layer structure of the NBIR pulse. The position of the maximum in NBIR concentrations below the 2000-m depth is similar between the two cases, does not change with time and is associated with the deep abyssal plain. The difference between the two simulations is most pronounced near the 2000-m depth (layer 34): The FULL_ADV simulation exhibits a strong NBIR pulse near approximately 15°N, whereas the MEAN_ADV pulse is much weaker and is located farther north.

b. Southern BIR tracer

Using the same concept as NBIR, the SBIR tracer quantifies the advective time scales and pathways of the signal propagation from the Southern Ocean into the Atlantic. Similar to the NBIR tracer, the SBIR pulse separates from the boundary, where it is being removed beginning at year 2, and moves with AMOC currents. The total SBIR inventory is, however, significantly less sensitive to the presence of mesoscale eddies, and the difference between the FULL_ADV and MEAN_ADV inventories at year 50 is only 17%. The main SBIR pathways are associated with the northward spread of the Antarctic Intermediate Water (AAIW) in the southwestern Atlantic, the Agulhas
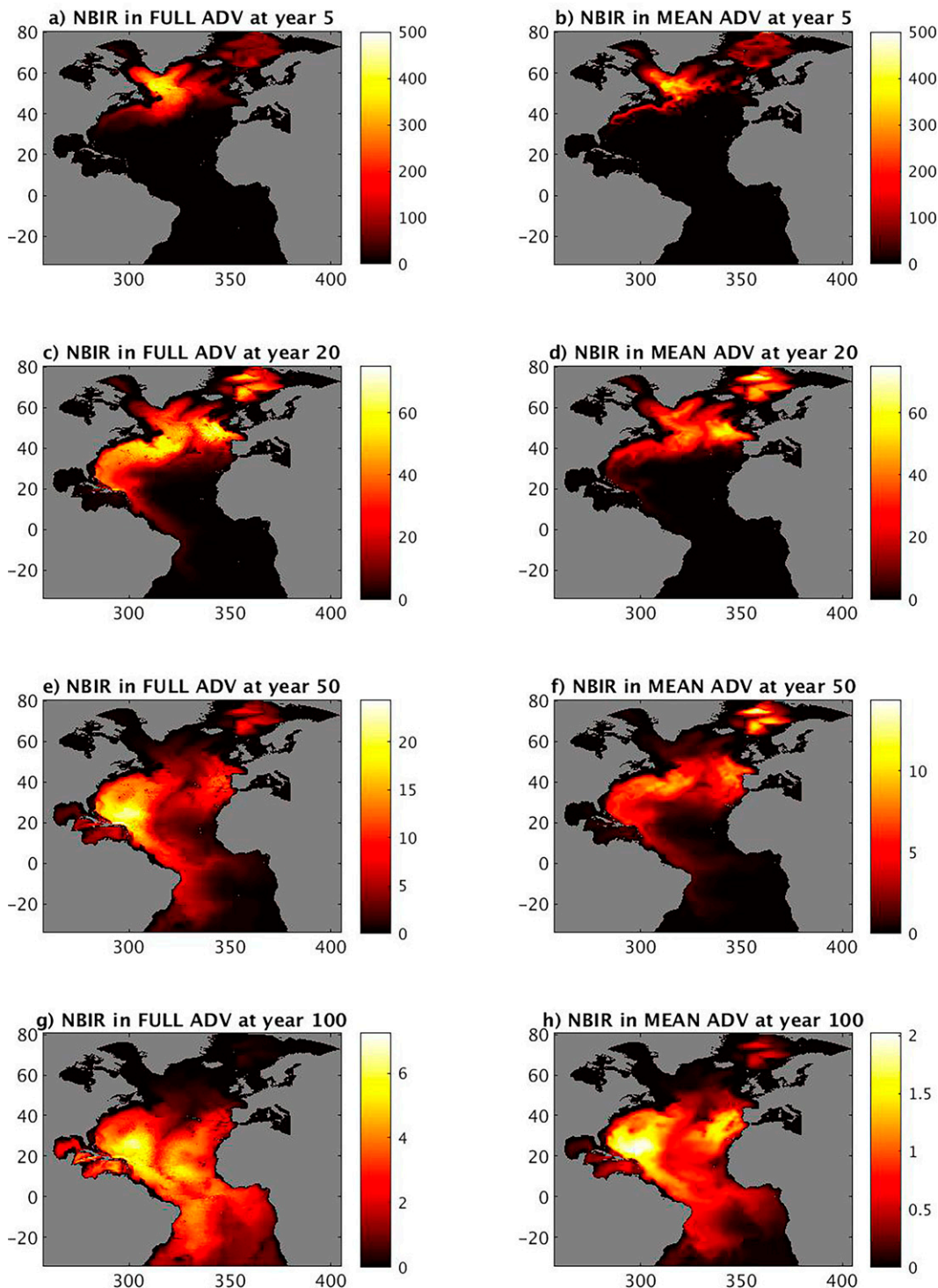
FIG. 4. Annual-mean inventory (vertical integral) of the NBIR tracer in (left) FULL_ADV and (right) MEAN_ADV. Note the different color scales in panels. The tracers are nondimensional, and the units of the inventory are meters.

leakage in the southeastern Atlantic and the propagation of the Antarctic Bottom Water (AABW) in the deepest layers. In our discussion, we will, therefore, distinguish between the upper 2000 m (layers 1–34) and deep layers below. Most of the SBIR tracer is found in the deep layers by the end of simulations: 53% in FULL_ADV and 56% in MEAN_ADV.

Propagation of the SBIR tracer in the deep layers is steered by major topographic features: the mid-Atlantic ridge, the
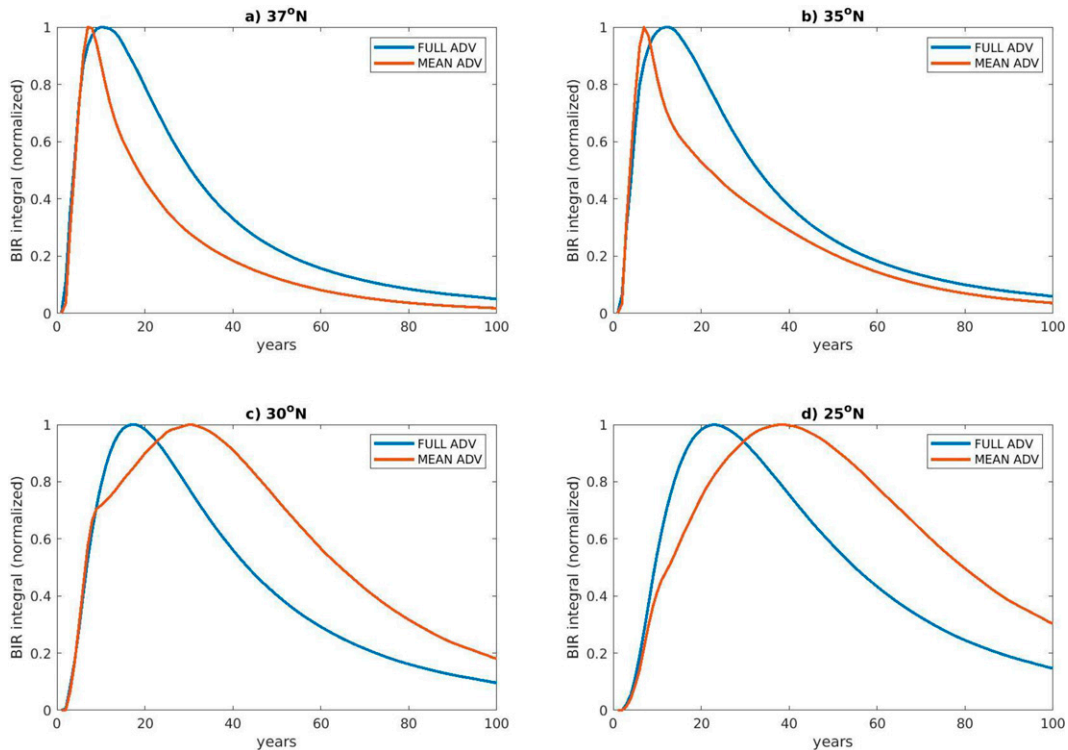
FIG. 5. Annual-mean zonal integrals of NBIR inventories at four different latitudes as functions of time. The integrals are calculated over 200 grid points (15.9° longitude) from the western boundary. For presentation purposes, each curve is divided by its maximum and smoothed in time by a 5-point running-mean filter.

Rio Grande Rise in the west, and the Walvis Ridge in the east. The SBIR tracer first enters the Atlantic domain in the southeast. The tracer initially fills the region south of the Walvis Ridge (Figs. 7a,b), within the eastern boundary, but is gradually transported out of the Atlantic due to the continuing water exchange with the Southern Ocean. These exchanges are facilitated in FULL_ADV by eddy-induced diffusive fluxes, which are nearly meridional in the southernmost part of the model domain (Fig. 2) and which explain smaller inventories of SBIR compared to MEAN_ADV. Starting at approximately year 10, we observe two deep pulses moving northward, one to the west and another to the east of the mid-Atlantic ridge. Assisted by the eddy-induced stirring, these deep tracer pulses propagate faster in FULL_ADV than in MEAN_ADV, although the overall difference is less pronounced than in the case of NBIR (Figs. 7c–f). Despite relatively large magnitudes of the eddy diffusivity in the South Atlantic, the direction of the eddy-induced stirring is primarily zonal north of 20°S (Fig. 2) and the position of the center of these deep tracer pulses is similar between the two simulations.

The SBIR tracer pulse is more spread out meridionally in the FULL_ADV simulation. By the end of the simulation, 40% of the tracer is found in the Northern Hemisphere, compared to only 20% in MEAN_ADV. The tracer moves faster in the upper layers, and the northward extent of the SBIR pulse is significantly larger in the upper 2000 m (Fig. 8). By

the end of the FULL_ADV simulation, most of the upper-layer tracer (58%) is found in the Northern Hemisphere. The distribution is more uniform vertically in MEAN_ADV, with 36% of the tracer in the upper layers found north of the equator.

5. Discussion and conclusions

Redistribution of tracer anomalies takes place along AMOC pathways that link the high-latitude North Atlantic with the midlatitudes and the Southern Ocean. Within the most basic schematic of a semiadabatic AMOC, these tracer anomalies enter and leave the Atlantic Ocean from the surface in the northern high latitudes and through lateral exchanges with the Southern Ocean. The conveyor belt concept, however, hides underlying complexity of a three-dimensional system of currents on a wide range of spatial scales. Our numerical study evaluates the importance of mesoscale currents (eddies) in these AMOC pathways and associated time scales. The contribution of eddies remains poorly understood, mainly because of challenges in studying these effects over large distances and long times. The offline tracer model used in this study overcomes this technical difficulty because it permits extended simulations at the relatively low computational cost. More important for the study is, however, the unique ability of offline simulations to isolate the direct contribution of eddies to the large-scale distribution of oceanic tracers. This task is achieved by a sensitivity run with a synthetic time-averaged
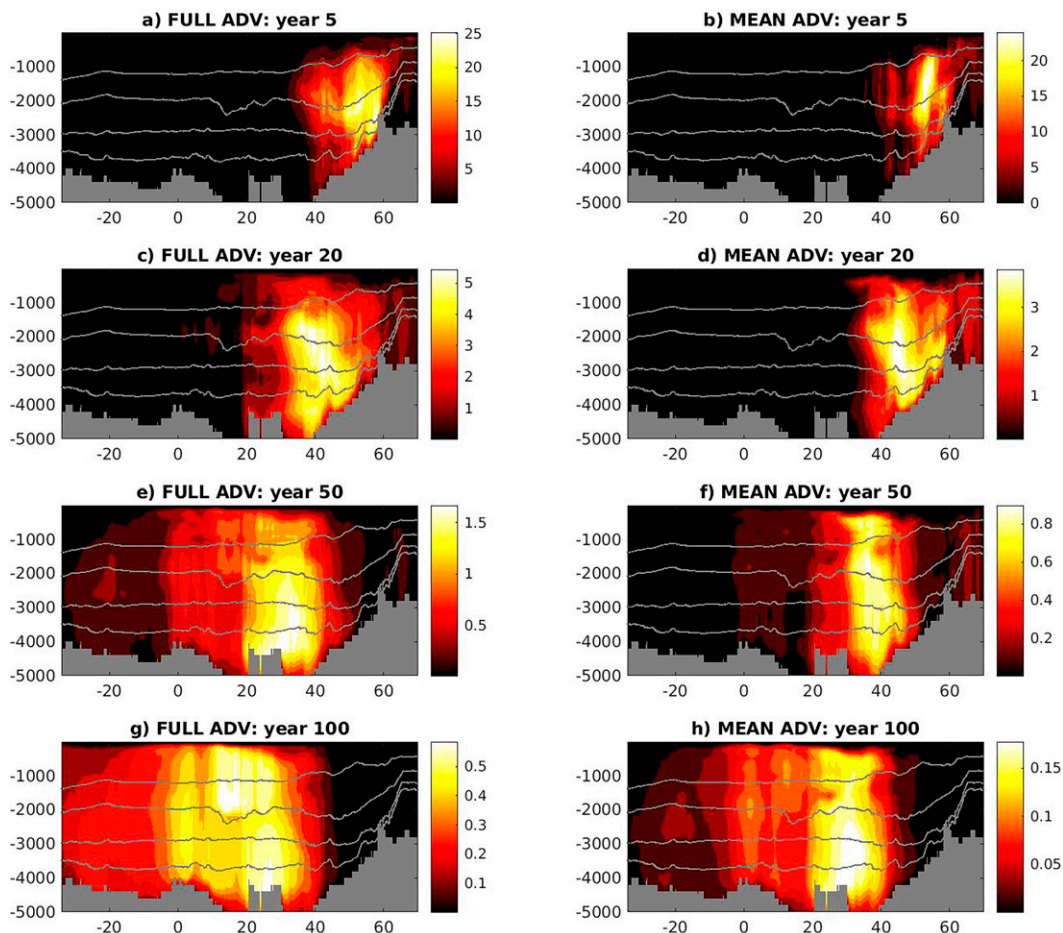
FIG. 6. Annual-mean zonal integral of the NBIR concentrations on the latitude–depth plane in (left) FULL_ADV and (right) MEAN_ADV. The tracer concentration is first integrated in the zonal direction and within each layer and then interpolated to z coordinates using zonal mean layer depth. The lines show the middepth of model layers 30, 34, 36, and 37, zonally and time averaged. Note differences in the color contour intervals; units are 10^4 m.

and spatially smoothed currents. The study considers two boundary impulse response (BIR) tracers, which can be used to quantify the importance of the Atlantic tracer exchanges with the high-latitude atmosphere in the north and with the Southern Ocean in the south. The results are interpreted using eddy-induced transport tensors, which are derived from lateral distributions of a separate set of idealized tracers.

The results provide several examples of the importance of eddies in propagation of BIR tracers. During the early stages of the simulation, eddy advection allows for more tracer to remain in the ocean and, thus, increases the overall BIR inventory. This effect can be interpreted as the eddy-induced enhancement of the overall ventilation. Specifically, eddies facilitate the removal of BIR away from the North Atlantic surface, where the waters are being continuously renewed and BIR tracer concentrations are being depleted by the atmosphere. It is not, however, easy to quantify this potentially important effect of eddies in our study. The stratification in the sensitivity simulation MEAN_ADV is different from the control run FULL_ADV and it would be difficult to claim that the difference in tracer

inventories observed here is due solely to mesoscale advection, despite the same vertical diffusivities in both simulations. In addition, at time scales longer than those considered in this study, the eddy-induced mixing can be expected to expose more tracer to the surface and thus facilitate tracer removal.

In agreement with an idealized leaky-pipe model, the eddies spread the tracer away from the main DWBC pathway, which increases the advective time scale within AMOC at the early stages. Zonal eddy-induced transports move the tracer over the mid-Atlantic Ridge to the eastern part of the domain, which helps to achieve more spatially uniform ventilation of the Atlantic interior. The eddy effects are not, however, limited to the eastward spreading of the tracer from the western boundary. The mesoscale currents also facilitate the meridional spreading of the NBIR tracer south of the eastward Gulf Stream extension and across the deep equatorial current farther south. In this sense, the eddies assist the large-scale advection, and the resulting meridional propagation of the NBIR pulse is noticeably faster in the presence of mesoscale currents. Similarly, the meridional propagation of
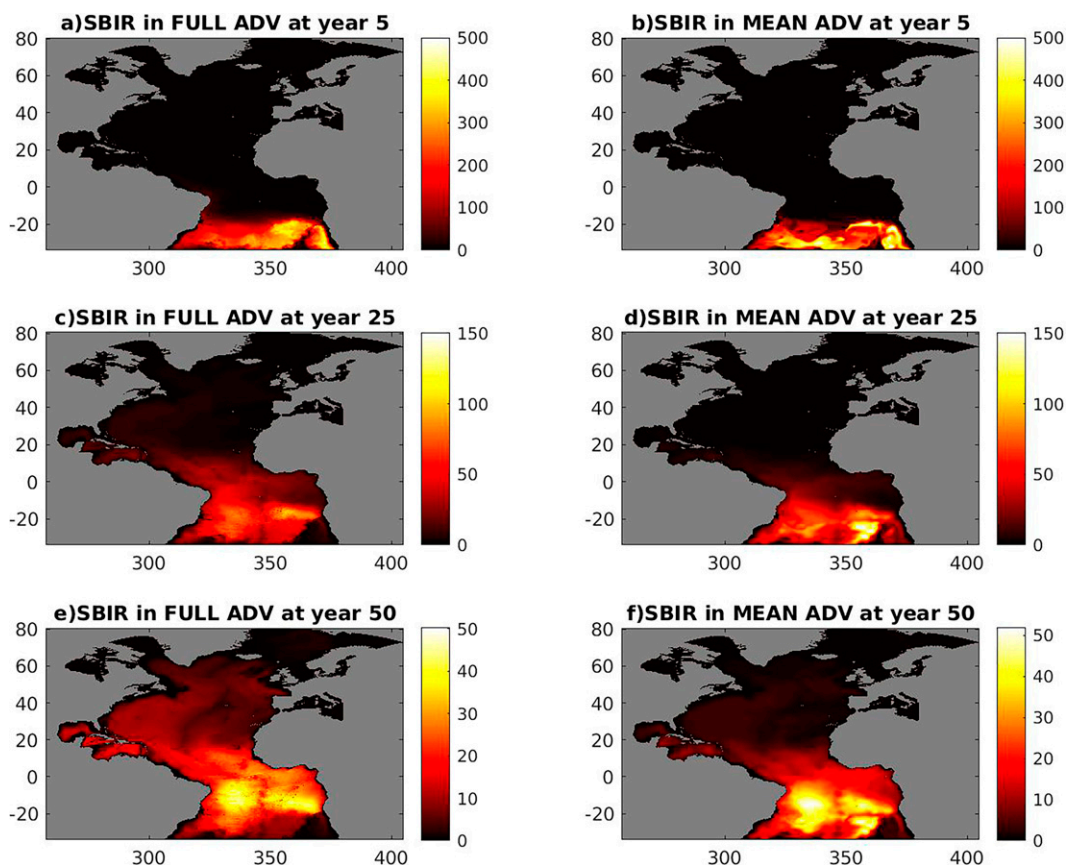
FIG. 7. Annual-mean inventory (vertical integral) of the SBIR tracer in (left) FULL_ADV and (right) MEAN_ADV. Note the different color scales in panels. The tracers are nondimensional, and the unit of the inventory is meters.

the SBIR tracer from the southern boundary of the Atlantic is also facilitated by mesoscale eddies.

The results also demonstrate the importance of spatial inhomogeneity and anisotropy of eddy-induced mixing, demonstrated by the eddy-induced diffusion and advection tensors. The anisotropy of the eddy diffusivity and the direction of the maximal eddy-induced dispersion are clearly important for the propagation of tracers within AMOC. For example, the eddy-induced stirring is primarily zonal in the mid- and low-latitude interior, far from the coasts and topographic features. Zonal mixing is also very strong in the South Atlantic (north of 20°S), and the resulting redistribution of temperature and salinity anomalies will help to establish a basinwide west–east density contrast, which is particularly important for the AMOC dynamics (Kamenkovich and Radko 2011). Nevertheless, the eddy-induced diffusion and advection have significant meridional components near the western boundary and in deep ocean layers, which assists the meridional propagation of the pulse. For example, a mixing hotspot in the vicinity of the eastward Gulf Stream extension helps to move the NBIR pulse southward of this location. An accurate calculation of the transport tensors is, however, challenging, due to uncertainty in tracer-based estimates of the eddy diffusivity revealed by previous studies (e.g., Bachman et al. 2020;

Kamenkovich et al. 2021; Sun et al. 2021) and should be interpreted with caution.

Eddy-induced diffusivities and the corresponding tracer transports are complex, but the significance of this complexity for large-scale tracer distributions remains unclear. This study combines an analysis of eddy-induced transport tensor and a direct inquiry into the importance of eddy-induced advection for tracer distribution. The time-independent transport tensor discussed in this study still lacks important temporal fluctuations (Haigh et al. 2020; Kamenkovich et al. 2021). The attempts to use the diagnosed eddy-induced diffusivities in place of eddies in our study was, however, unsuccessful due to numerical instability. The instability was most likely caused by negative and large positive values of diffusivity and the presence of sharp gradients in high-resolution simulations. An alternative approach of using coarse-resolution simulations with parameterized tracer transports would involve different large-scale circulation, leading to additional challenges with interpretation.

Most notable challenge in any analysis of mesoscale dynamics is the lack of a clear scale separation between the large-scale AMOC and mesoscale currents. Time-based definitions of mesoscale variability complicate its separation from the seasonal cycle in the large-scale fields, and the simple 5-yr time average used in this study assumes that seasonal anomalies in AMOC
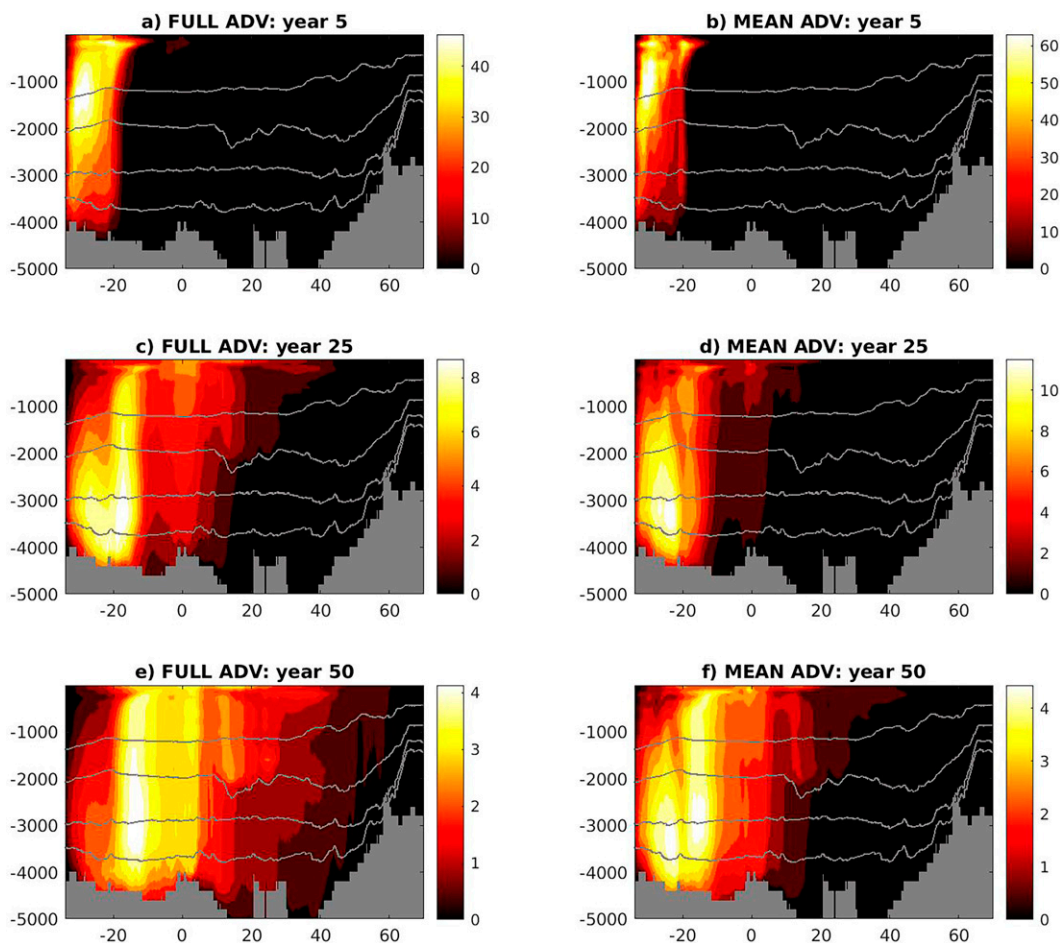
FIG. 8. Annual-mean zonal integral of the SBIR concentrations on the latitude–depth plane in (left) FULL_ADV and (right) MEAN_ADV. The tracer concentration is first integrated in the zonal direction and within each layer and then interpolated to z coordinates using the zonal mean layer depth. The lines show the middepth of model layers 30, 34, 36, and 37, zonally and time averaged. Note differences in the color contour intervals; units are 10^4 m.

are weaker than the mesoscale currents. On the other hand, definitions based on a spatial scale, also used in this study, result in additional eddy-induced terms in the tracer budgets (e.g., Sun et al. 2021). At the same time, a spatial scale-based approach seems like a natural way to define mesoscale anomalies missing in coarse-resolution ocean models.

This study focuses on the direct contribution of eddy-induced tracer fluxes, by assuming that the large-scale circulation is the same in both simulations. The important effects of eddies on large-scale currents are, therefore, outside the scope of this study. For example, the eddies have been shown to play a key role in the dynamics of western boundary currents and their eastward extensions (e.g., Shevchenko and Berloff 2015; Waterman et al. 2011) and midlatitude stratification (Henning and Vallis 2004). In addition, eddy-induced zonal jets (Kamenkovich et al. 2009; Maximenko et al. 2008) are shown to be important for spreading of the ventilation signal to the eastern part of the deep Atlantic. The absence of these eddy-driven currents in coarse-resolution models will, therefore, further increase model biases in tracer distributions.

Finally, mesoscale and submesoscale currents can also be expected to play a role in the variability of the mixed layer depth which has been shown to modulate the air–sea heat exchanges (Tozuka and Cronin 2014; Gao et al. 2022), and submesoscale currents, which are missing in our study, can be particularly important for ventilation (Callies et al. 2015). Studies of the importance of eddy-induced advection for tracer distribution should clearly be continued, as they are needed for evaluation of eddy-permitting simulations that stop short of full resolution of mesoscale, as well as for development of eddy parameterization schemes.

Data availability statement. Data used for the main analysis and figures in the paper are openly available from a public repository at https://doi.org/10.17604/cbrf-1s25. Complete data from numerical simulations will be made available upon request. There are no restrictions on the data use.

APPENDIX

Calculation of the Eddy Transport Tensor

Eighteen overlapping 110-day-long simulations are carried out, with each consecutive segment starting 10 days before the end of the previous one. Four idealized conservative tracers were initialized with the following analytical horizontal profiles:

$$c_1 = 1 - \frac{n_x}{N_x}, \ c_2 = 1 - \frac{n_y}{N_y}$$

$$c_3 = \left(\frac{n_x - N_x/2}{N_x/2}\right)^2 + \left(\frac{n_y - N_y/2}{N_y/2}\right)^2, \ c_4 = \cos\left(\frac{\pi n_x}{720}\right)\cos\left(\frac{\pi n_y}{720}\right),$$

(A1)

where $n_x = 1, \dots, N_x$ and $n_y = 1, \dots, N_y$ are grid indices in the zonal and meridional directions and $N_x = 1475$ and $N_y = 1950$ are the total number of grid points in each corresponding direction. Each of these profiles is multiplied by the following "hat function" $h(n_y)$, in order to minimize the effects of the open boundaries:

$$h(n_y) = \begin{cases} \exp\left[-\left(\frac{n_y - 925}{700}\right)^6\right], & 50 < n_y < 1800 \\ 0, & \text{otherwise} \end{cases} \quad (A2)$$

The initial tracer concentrations (A1) and (A2) are uniform vertically. The tracers do not have internal sources and sinks, and their surface fluxes are zero.

We use the optimization technique with Tikhonov regularization (Li et al. 2006) to extract the divergent component in eddy fluxes. The method minimizes the opposing nonrotational and nondivergent components in $\mathbf{F}_{div}$ and $(\mathbf{F}_e - \mathbf{F}_{div})$. These components cancel each other in the sum $\mathbf{F}_e$ but cause ambiguity in defining $\mathbf{F}_{div}$ and $\mathbf{F}_{rot}$. The main advantage of this method for our study is that it avoids the need for boundary conditions, which are particularly ambiguous at the open boundaries. Note that the decomposition preserves boundary values of $\mathbf{F}_e$.

The finite-difference form of Eq. (6) is first written in the following matrix form

$$\mathbf{y} = \mathbf{A}\mathbf{x}, \text{ where } \mathbf{y} = \begin{pmatrix} F_x \\ F_y \end{pmatrix} \text{ and } \mathbf{x} = \begin{pmatrix} \Phi \\ \Psi \end{pmatrix}. \quad (A3)$$

The solution for $\mathbf{y}$ is then obtained by minimizing the objective functional

$$J_\alpha(\mathbf{x}) = \frac{1}{2}(\mathbf{y} - \mathbf{A}\mathbf{x})^T(\mathbf{y} - \mathbf{A}\mathbf{x}) + \alpha\frac{1}{2}\mathbf{x}^T\mathbf{x}, \quad (A4)$$

where "T" stands for the transpose, and the regularization parameter $\alpha = 10^{-15} \text{ m}^{-2}$. Minimization of the regularization

term (second term on the right-hand side) is equivalent to minimizing the opposing irrotational, nondivergent components of flux that cause uncertainty in the decomposition (Li et al. 2006). We use the quasi-Newton method with limited memory Broydon–Fletcher–Goldfarb–Shanno (BFGS) updating (a bulti-in MATLAB function). Equation (4) is solved locally by matrix division function in MATLAB, which determines the solution in the least squares sense to the overdetermined system of equations.

REFERENCES

Abernathey, R., and J. Marshall, 2013: Global surface eddy diffusivities derived from satellite altimetry. *J. Geophys. Res. Oceans*, **118**, 901–916, https://doi.org/10.1002/jgrc.20066.

——, D. Ferreira, and A. Klocker, 2013: Diagnostics of isopycnal mixing in a circumpolar channel. *Ocean Modell.*, **72**, 1–16, https://doi.org/10.1016/j.ocemod.2013.07.004.

Bachman, S. D., D. P. Marshall, J. R. Maddison, and J. Mak, 2017: Evaluation of a scalar eddy transport coefficient based on geometric constraints. *Ocean Modell.*, **109**, 44–54, https://doi.org/10.1016/j.ocemod.2016.12.004.

——, B. Fox-Kemper, and F. O. Bryan, 2020: A diagnosis of anisotropic eddy diffusion from a high-resolution global ocean model. *J. Adv. Model. Earth Syst.*, **12**, e2019MS001904, https://doi.org/10.1029/2019MS001904.

Bleck, R., 2002: An oceanic general circulation model framed in hybrid isopycnic-Cartesian coordinates. *Ocean Modell.*, **4**, 55–88, https://www.sciencedirect.com/science/article/abs/pii/S1463500301000129; Corrigendum, **4**, 219, https://doi.org/10.1016/S1463-5003(01)00017-8.

——, C. Rooth, D. M. Hu, and L. T. Smith, 1992: Salinity-driven thermocline transients in a wind-forced and thermohaline-forced isopycnic coordinate model of the north-Atlantic. *J. Phys. Oceanogr.*, **22**, 1486–1505, https://doi.org/10.1175/1520-0485(1992)022<1486:SDTTIA>2.0.CO;2.

Booth, J., and I. Kamenkovich, 2008: Isolating the role of mesoscale eddies in mixing of a passive tracer in an eddy resolving model. *J. Geophys. Res. Oceans*, **113**, C05021, https://doi.org/10.1029/2007JC004510.

Broecker, W. S., 1997: Thermohaline circulation, the Achilles heel of our climate system: Will man-made CO_2 upset the current balance? *Science*, **278**, 1582–1588, https://doi.org/10.1126/science.278.5343.1582.

Bryan, F., 1987: Parameter sensitivity of primitive equation ocean general-circulation models. *J. Phys. Oceanogr.*, **17**, 970–985, https://doi.org/10.1175/1520-0485(1987)017<0970:PSOPEO>2.0.CO;2.

Callies, J., R. Ferrari, J. M. Klymak, and J. Gula, 2015: Seasonality in submesoscale turbulence. *Nat. Commun.*, **6**, 6862, https://doi.org/10.1038/ncomms7862.

Cessi, P., and M. Fantini, 2004: The eddy-driven thermocline. *J. Phys. Oceanogr.*, **34**, 2642–2658, https://doi.org/10.1175/JPO2657.1.

Chassignet, E. P., L. T. Smith, G. R. Halliwell, and R. Bleck, 2003: North Atlantic simulations with the Hybrid Coordinate Ocean Model (HYCOM): Impact of the vertical coordinate choice, reference pressure, and thermobaricity. *J. Phys. Oceanogr.*, **33**, 2504–2526, https://doi.org/10.1175/1520-0485(2003)033<2504:NASWTH>2.0.CO;2.

Chelton, D. B., R. A. DeSzoeke, M. G. Schlax, K. El Naggar, and N. Siwertz, 1998: Geographical variability of the first baroclinic Rossby radius of deformation. *J. Phys. Oceanogr.*,

28, 433–460, https://doi.org/10.1175/1520-0485(1998)028<0433:GVOTFB>2.0.CO;2.

Doney, S. C., and Coauthors, 2004: Evaluating global ocean carbon models: The importance of realistic physics. *Global Biogeochem. Cycles*, **18**, GB3017, https://doi.org/10.1029/2003GB002150.

Dutay, J. C., and Coauthors, 2002: Evaluation of ocean model ventilation with CFC-11: Comparison of 13 global ocean models. *Ocean Modell.*, **4**, 89–120, https://doi.org/10.1016/S1463-5003(01)00013-0.

Fox-Kemper, B., R. Ferrari, and J. Pedlosky, 2003: On the indeterminacy of rotational and divergent eddy fluxes. *J. Phys. Oceanogr.*, **33**, 478–483, https://doi.org/10.1175/1520-0485(2003)033<0478:OTIORA>2.0.CO;2.

Gao, Y., I. Kamenkovich, N. Perlin, and B. Kirtman, 2022: Oceanic advection controls mesoscale mixed layer heat budget and air-sea heat exchange in the Southern Ocean. *J. Phys. Oceanogr.*, **52**, 537–555, https://doi.org/10.1175/JPO-D-21-0063.1.

Gent, P. R., and J. C. McWilliams, 1990: Isopycnal mixing in ocean circulation models. *J. Phys. Oceanogr.*, **20**, 150–155, https://doi.org/10.1175/1520-0485(1990)020<0150:IMIOCM>2.0.CO;2.

Gnanadesikan, A., 1999: A simple predictive model for the structure of the oceanic pycnocline. *Science*, **283**, 2077–2079, https://doi.org/10.1126/science.283.5410.2077.

——, J. P. Dunne, R. M. Key, K. Matsumoto, J. L. Sarmiento, R. D. Slater, and P. S. Swathi, 2004: Oceanic ventilation and biogeochemical cycling: Understanding the physical mechanisms that produce realistic distributions of tracers and productivity. *Global Biogeochem. Cycles*, **18**, GB4010, https://doi.org/10.1029/2003GB002097.

——, D. Bianchi, and M. A. Pradal, 2013: Critical role for mesoscale eddy diffusion in supplying oxygen to hypoxic ocean waters. *Geophys. Res. Lett.*, **40**, 5194–5198, https://doi.org/10.1002/grl.50998.

——, M. A. Pradal, and R. Abernathey, 2015: Isopycnal mixing by mesoscale eddies significantly impacts oceanic anthropogenic carbon uptake. *Geophys. Res. Lett.*, **42**, 4249–4255, https://doi.org/10.1002/2015GL064100.

Grist, J. P., R. Marsh, and S. A. Josey, 2009: On the relationship between the north Atlantic meridional overturning circulation and the surface-forced overturning streamfunction. *J. Climate*, **22**, 4989–5002, https://doi.org/10.1175/2009JCLI2574.1.

Haigh, M., and P. Berloff, 2021: On co-existing diffusive and antidiffusive tracer transport by oceanic mesoscale eddies. *Ocean Modell.*, **168**, 101909, https://doi.org/10.1016/j.ocemod.2021.101909.

——, L. Sun, I. Shevchenko, and P. Berloff, 2020: Tracer-based estimates of eddy-induced diffusivities. *Deep-Sea Res. I*, **160**, 103264, https://doi.org/10.1016/j.dsr.2020.103264.

——, L. L. Sun, J. C. McWilliams, and P. Berloff, 2021a: On eddy transport in the ocean. Part I: The diffusion tensor. *Ocean Modell.*, **164**, 101831, https://doi.org/10.1016/j.ocemod.2021.101831.

——, ——, ——, and ——, 2021b: On eddy transport in the ocean. Part II: The advection tensor. *Ocean Modell.*, **165**, 101845, https://doi.org/10.1016/j.ocemod.2021.101845.

Haine, T. W. N., and T. M. Hall, 2002: A generalized transport theory: Water-mass composition and age. *J. Phys. Oceanogr.*, **32**, 1932–1946, https://doi.org/10.1175/1520-0485(2002)032<1932:AGTTWM>2.0.CO;2.

Halliwell, G. R., 2004: Evaluation of vertical coordinate and vertical mixing algorithms in the HYbrid-Coordinate Ocean Model (HYCOM). *Ocean Modell.*, **7**, 285–322, https://doi.org/10.1016/j.ocemod.2003.10.002.

Han, M., I. Kamenkovich, T. Radko, and W. E. Johns, 2013: Relationship between air–sea density flux and isopycnal meridional overturning circulation in a warming climate. *J. Climate*, **26**, 2683–2699, https://doi.org/10.1175/JCLI-D-11-00682.1.

Henning, C. C., and G. K. Vallis, 2004: The effects of mesoscale eddies on the main subtropical thermocline. *J. Phys. Oceanogr.*, **34**, 2428–2443, https://doi.org/10.1175/JPO2639.1.

Holzer, M., and T. M. Hall, 2000: Transit-time and tracer-age distributions in geophysical flows. *J. Atmos. Sci.*, **57**, 3539–3558, https://doi.org/10.1175/1520-0469(2000)057<3539:TTATAD>2.0.CO;2.

Huang, B. Y., P. H. Stone, A. P. Sokolov, and I. V. Kamenkovich, 2003: Ocean heat uptake in transient climate change: Mechanisms and uncertainty due to subgrid-scale eddy mixing. *J. Climate*, **16**, 3344–3356, https://doi.org/10.1175/1520-0442(2003)016<3344:OHUITC>2.0.CO;2.

Jayne, S. R., and J. Marotzke, 2002: The oceanic eddy heat transport. *J. Phys. Oceanogr.*, **32**, 3328–3345, https://doi.org/10.1175/1520-0485(2002)032<3328:TOEHT>2.0.CO;2.

Kamenkovich, I., and T. Radko, 2011: Role of the Southern Ocean in setting the Atlantic stratification and meridional overturning circulation. *J. Mar. Res.*, **69**, 277–308, https://doi.org/10.1357/002224011798765286.

——, P. Berloff, and J. Pedlosky, 2009: Anisotropic material transport by eddies and eddy-driven currents in a model of the north Atlantic. *J. Phys. Oceanogr.*, **39**, 3162–3175, https://doi.org/10.1175/2009JPO4239.1.

——, I. I. Rypina, and P. Berloff, 2015: Properties and origins of the anisotropic eddy-induced transport in the north Atlantic. *J. Phys. Oceanogr.*, **45**, 778–791, https://doi.org/10.1175/JPO-D-14-0164.1.

——, Z. Garraffo, R. Pennel, and R. A. Fine, 2017: Importance of mesoscale eddies and mean circulation in ventilation of the Southern Ocean. *J. Geophys. Res. Oceans*, **122**, 2724–2741, https://doi.org/10.1002/2016JC012292.

——, P. Berloff, M. Haigh, L. L. Sun, and Y. Y. Lu, 2021: Complexity of mesoscale eddy diffusivity in the ocean. *Geophys. Res. Lett.*, **48**, e2020GL091719, https://doi.org/10.1029/2020GL091719.

Khatiwala, S., M. Visbeck, and P. Schlosser, 2001: Age tracers in an ocean GCM. *Deep-Sea Res. I*, **48**, 1423–1441, https://doi.org/10.1016/S0967-0637(00)00094-7.

——, F. Primeau, and T. Hall, 2009: Reconstruction of the history of anthropogenic CO_2 concentrations in the ocean. *Nature*, **462**, 346–349, https://doi.org/10.1038/nature08526.

Kostov, Y., K. C. Armour, and J. Marshall, 2014: Impact of the Atlanticmeridional overturning circulation on ocean heat storage and transient climate change. *Geophys. Res. Lett.*, **41**, 2108–2116, https://doi.org/10.1002/2013GL058998.

Kuhlbrodt, T., and J. M. Gregory, 2012: Ocean heat uptake and its consequences for the magnitude of sea level rise and climate change. *Geophys. Res. Lett.*, **39**, L18608, https://doi.org/10.1029/2012GL052952.

Large, W. G., J. C. Mcwilliams, and S. C. Doney, 1994: Oceanic vertical mixing – A review and a model with a nonlocal boundary-layer parameterization. *Rev. Geophys.*, **32**, 363–403, https://doi.org/10.1029/94RG01872.

Lau, N. C., and J. M. Wallace, 1979: Distribution of horizontal transports by transient eddies in the northern hemisphere wintertime circulation. *J. Atmos. Sci.*, **36**, 1844–1861, https://doi.org/10.1175/1520-0469(1979)036<1844:OTDOHT>2.0.CO;2.

Ledwell, J. R., A. J. Watson, and C. S. Law, 1993: Evidence for slow mixing across the pycnocline from an open-ocean tracer-release experiment. *Nature*, **364**, 701–703, https://doi.org/10.1038/364701a0.

Li, Z. J., Y. Chao, and J. C. McWilliams, 2006: Computation of the streamfunction and velocity potential for limited and irregular domains. *Mon. Wea. Rev.*, **134**, 3384–3394, https://doi.org/10.1175/MWR3249.1.

Lumpkin, R., and K. Speer, 2007: Global ocean meridional overturning. *J. Phys. Oceanogr.*, **37**, 2550–2562, https://doi.org/10.1175/JPO3130.1.

Maddison, J. R., D. P. Marshall, and J. Shipton, 2015: On the dynamical influence of ocean eddy potential vorticity fluxes. *Ocean Modell.*, **92**, 169–182, https://doi.org/10.1016/j.ocemod.2015.06.003.

Maltrud, M., F. Bryan, and S. Peacock, 2010: Boundary impulse response functions in a century-long eddying global ocean simulation. *Environ. Fluid Mech.*, **10**, 275–295, https://doi.org/10.1007/s10652-009-9154-3.

Marshall, J., and G. Shutts, 1981: A note on rotational and divergent eddy fluxes. *J. Phys. Oceanogr.*, **11**, 1677–1680, https://doi.org/10.1175/1520-0485(1981)011<1677:ANORAD>2.0.CO;2.

——, and T. Radko, 2003: Residual-mean solutions for the Antarctic Circumpolar Current and its associated overturning circulation. *J. Phys. Oceanogr.*, **33**, 2341–2354, https://doi.org/10.1175/1520-0485(2003)033<2341:RSFTAC>2.0.CO;2.

——, J. R. Scott, K. C. Armour, J. M. Campin, M. Kelley, and A. Romanou, 2015: The ocean's role in the transient response of climate to abrupt greenhouse gas forcing. *Climate Dyn.*, **44**, 2287–2299, https://doi.org/10.1007/s00382-014-2308-0.

Maximenko, N. A., O. V. Melnichenko, P. P. Niiler, and H. Sasaki, 2008: Stationary mesoscale jet-like features in the ocean. *Geophys. Res. Lett.*, **35**, L08603, https://doi.org/10.1029/2008GL033267.

Munk, W. H., 1966: Abyssal recipes. *Deep-Sea Res. Oceanogr. Abstr.*, **13**, 707–730, https://doi.org/10.1016/0011-7471(66)90602-4.

Peacock, S., and M. Maltrud, 2006: Transit-time distributions in a global ocean model. *J. Phys. Oceanogr.*, **36**, 474–495, https://doi.org/10.1175/JPO2860.1.

Radko, T., and J. Marshall, 2004: The leaky thermocline. *J. Phys. Oceanogr.*, **34**, 1648–1662, https://doi.org/10.1175/1520-0485(2004)034<1648:TLT>2.0.CO;2.

——, I. Kamenkovich, and P. Y. Dare, 2008: Inferring the pattern of the oceanic meridional transport from the air–sea density flux. *J. Phys. Oceanogr.*, **38**, 2722–2738, https://doi.org/10.1175/2008JPO3748.1.

Roberts, M. J., and D. P. Marshall, 2000: On the validity of downgradient eddy closures in ocean models. *J. Geophys. Res.*, **105**, 28 613–28 627, https://doi.org/10.1029/1999JC000041.

Rypina, I. I., I. Kamenkovich, P. Berloff, and L. J. Pratt, 2012: Eddy-induced particle dispersion in the near-surface north Atlantic. *J. Phys. Oceanogr.*, **42**, 2206–2228, https://doi.org/10.1175/JPO-D-11-0191.1.

Samelson, R. M., 2004: Simple mechanistic models of middepth meridional overturning. *J. Phys. Oceanogr.*, **34**, 2096–2103, https://doi.org/10.1175/1520-0485(2004)034<2096:SMMOMM>2.0.CO;2.

Sen Gupta, A., and M. H. England, 2004: Evaluation of interior circulation in a high-resolution global ocean model. Part I: Deep and bottom waters. *J. Phys. Oceanogr.*, **34**, 2592–2614, https://doi.org/10.1175/JPO2651.1.

Sevellec, F., and A. V. Fedorov, 2011: Stability of the Atlantic meridional overturning circulation and stratification in a zonally averaged ocean model: Effects of freshwater flux, Southern Ocean winds, and diapycnal diffusion. *Deep-Sea Res. II*, **58**, 1927–1943, https://doi.org/10.1016/j.dsr2.2010.10.070.

Shevchenko, I. V., and P. S. Berloff, 2015: Multi-layer quasi-geostrophic ocean dynamics in eddy-resolving regimes. *Ocean Modell.*, **94**, 1–14, https://doi.org/10.1016/j.ocemod.2015.07.018.

Smeed, D. A., and Coauthors, 2014: Observed decline of the Atlantic meridional overturning circulation 2004-2012. *Ocean Sci.*, **10**, 29–38, https://doi.org/10.5194/os-10-29-2014.

Stouffer, R. J., and Coauthors, 2006: Investigating the causes of the response of the thermohaline circulation to past and future climate changes. *J. Climate*, **19**, 1365–1387, https://doi.org/10.1175/JCLI3689.1.

Sun, L. L., M. Haigh, I. Shevchenko, P. Berloff, and I. Kamenkovich, 2021: On non-uniqueness of the mesoscale eddy diffusivity. *J. Fluid Mech.*, **920**, A32, https://doi.org/10.1017/jfm.2021.472.

Sun, S., and R. Bleck, 2001: Thermohaline circulation studies with an Isopycnic Coordinate Ocean Model. *J. Phys. Oceanogr.*, **31**, 2761–2782, https://doi.org/10.1175/1520-0485(2001)031<2761:TCSWAI>2.0.CO;2.

——, ——, C. Rooth, J. Dukowicz, E. Chassignet, and P. Killworth, 1999: Inclusion of thermobaricity in isopycnic-coordinate ocean models. *J. Phys. Oceanogr.*, **29**, 2719–2729, https://doi.org/10.1175/1520-0485(1999)029<2719:IOTIIC>2.0.CO;2.

Toggweiler, J. R., and B. Samuels, 1998: On the ocean's large-scale circulation near the limit of no vertical mixing. *J. Phys. Oceanogr.*, **28**, 1832–1852, https://doi.org/10.1175/1520-0485(1998)028<1832:OTOSLS>2.0.CO;2.

Toole, J. M., K. L. Polzin, and R. W. Schmitt, 1994: Estimates of diapycnal mixing in the abyssal ocean. *Science*, **264**, 1120–1123, https://doi.org/10.1126/science.264.5162.1120.

Tozuka, T., and M. F. Cronin, 2014: Role of mixed layer depth in surface frontogenesis: The Agulhas Return Current front. *Geophys. Res. Lett.*, **41**, 2447–2453, https://doi.org/10.1002/2014GL059624.

Waterman, S., N. G. Hogg, and S. R. Jayne, 2011: Eddy–mean flow interaction in the Kuroshio Extension region. *J. Phys. Oceanogr.*, **41**, 1182–1208, https://doi.org/10.1175/2010JPO4564.1.

Waugh, D. W., and T. M. Hall, 2005: Propagation of tracer signals in boundary currents. *J. Phys. Oceanogr.*, **35**, 1538–1552, https://doi.org/10.1175/JPO2779.1.

Wolfe, C. L., and P. Cessi, 2010: What sets the strength of the middepth stratification and overturning circulation in eddying ocean models? *J. Phys. Oceanogr.*, **40**, 1520–1538, https://doi.org/10.1175/2010JPO4393.1.

Yeager, S., and G. Danabasoglu, 2014: The origins of late-twentieth-century variations in the large-scale North Atlantic circulation. *J. Climate*, **27**, 3222–3247, https://doi.org/10.1175/JCLI-D-13-00125.1.

Zalesak, S. T., 1979: Fully multidimensional flux-corrected transport algorithms for fluids. *J. Comput. Phys.*, **31**, 335–362, https://doi.org/10.1016/0021-9991(79)90051-2.